



Satellite-based midlatitude cyclone statistics over the Southern Ocean:

2. Tracks and surface fluxes

Xiaojun Yuan,¹ Jérôme Patoux,² and Cuihua Li¹

Received 29 July 2008; revised 24 November 2008; accepted 16 December 2008; published 19 February 2009.

[1] Midlatitude cyclone tracks over the Southern Ocean are constructed for the 1999–2006 period using two surface data sets: European Centre for Medium-range Weather Forecasts (ECMWF) sea-level pressure analyses on one hand, and on the other hand modified analyses in which high-wavenumber pressure variability derived from scatterometer swaths has been injected with a wavelet-based method. A comparison of track statistics reveals the differences between the two data sets. The fluxes of momentum and sensible and latent heat associated with these midlatitude cyclones are calculated and sorted by life span. Three aspects of these cyclone flux statistics are investigated. (1) The momentum flux into the ocean is stronger inside cyclones than over the rest of the Southern Ocean, while the ocean loses more sensible and latent heat outside of the cyclones. (2) The momentum flux into the ocean and the loss of sensible and latent heat by the ocean are larger when calculated from the scatterometer-modified analyses than when calculated from the original ECMWF analyses. (3) Mesoscale cyclones (short-lived cyclones) contribute a significant amount of the fluxes between the atmosphere and the Southern Ocean, although over slightly different geographic areas from longer-lived cyclones.

Citation: Yuan, X., J. Patoux, and C. Li (2009), Satellite-based midlatitude cyclone statistics over the Southern Ocean: 2. Tracks and surface fluxes, *J. Geophys. Res.*, 114, D04106, doi:10.1029/2008JD010874.

1. Introduction

[2] The air-sea exchanges of momentum, sensible and latent heat are an important component of the climate system. The momentum flux into the ocean is a key component of Ekman pumping, upwelling, wave activity and upper ocean mixing, as well as the large-scale ocean circulation. The air-sea heat fluxes play an important role in the redistribution of heat between the tropics and the poles. Determining the exchanges of momentum, sensible and latent heat between the Southern Ocean and the overlying atmosphere is crucial to understand the role played by the Southern Ocean in the global climate system on seasonal to interannual timescales.

[3] A unique characteristic of the Southern Hemisphere is the presence of the ice-covered Antarctic continent and surrounding sea ice. Coupled with the polar vortex, this distribution of glacial ice and sea ice feeds extremely cold air into the midlatitudes. The channeling of this cold air to the north is partly influenced by katabatic winds and the orography of the Antarctic continent, and partly controlled by the hemispheric distribution of synoptic weather systems, as it feeds the cold sector of midlatitude cyclones [Bromwich and Parish, 1998]. Once over relatively warmer water, the cold Antarctic air is responsible for intense upward heat fluxes. Moreover, the

baroclinicity caused by the strong temperature contrast between sea ice and open water, as well as the instability caused by cold air over relatively warmer water, provide ideal environments for cyclogenesis, which makes the seasonal ice zone a brewing ground for cyclones [Carrasco and Bromwich, 1993; Godfred-Spinning and Simmonds, 1996; Yuan *et al.*, 1999]. The rich cyclone activity over the Southern Ocean further complicates momentum and heat fluxes at the air-sea interface.

[4] Another characteristic of the Southern Ocean is the absence of blocking continent at high latitude and the existence of the Antarctic Circumpolar Current (ACC), which transports momentum and heat very efficiently around the entire Southern Hemisphere. Understanding the variability of local air-sea fluxes is thus important for our understanding of the variability of the entire Southern Ocean and, through the thermohaline circulation, of the global climate system.

[5] Existing statistics of these fluxes rely on bulk parameterizations and numerical weather prediction (NWP) model analyses of the surface wind field. Satellite data such as Special Sensor Microwave/Imager (SSM/I) measurements have been assimilated in some of these analyses or reanalyses [Kubota *et al.*, 2003]. However, the surface wind fields are often underestimated, especially in the high wind speed regime [Yuan, 2004]. Consequently, air-sea fluxes, which are a function of the surface wind speed, are also underestimated, in particular within midlatitude storms, where the surface wind speed is often higher than 20 m s^{-1} . Additionally, NWP models misrepresent a certain percentage of the midlatitude cyclones in the Southern Hemisphere: they either represent

¹Lamont-Doherty Earth Observatory of Columbia University, Palisades, New York, USA.

²Department of Atmospheric Sciences, University of Washington, Seattle, Washington, USA.

the intensity or structure of the pressure field incorrectly, or miss the incipient cyclone altogether [Hilburn *et al.*, 2003]. This further contributes to underestimating the impact of midlatitude cyclones on air-sea fluxes of momentum, sensible and latent heat. To characterize better these fluxes, we need to capture better the structure of the surface wind field, in particular the signature of extratropical cyclones, and assess better the impact of these cyclones on the ocean. It is therefore important to build an accurate picture of the number and intensity of cyclones and to understand their role in the exchange of energy between the atmosphere and the ocean. Simmonds and Keay [2002] performed such an analysis for the North Pacific and North Atlantic oceans, in which they computed the variability of the surface stress (approximated as the square of the surface wind speed) and compared it to variations in midlatitude cyclone characteristics. Here we assess the impact of satellite observations on the calculation of momentum and heat fluxes inside cyclones. To take advantage of high-resolution satellite observations while avoiding the discontinuity in storm tracking introduced by satellite swath gaps, we enhance NWP model sea-level pressure (SLP) analyses with SLP fields derived from scatterometer winds via a planetary boundary layer (PBL) model.

[6] Patoux *et al.* [2009] (hereafter PYL) described how to use SLP fields derived from QuikSCAT (QS) scatterometer winds using the University of Washington planetary boundary layer (UWPBL) model [Brown and Levy, 1986; Brown and Liu, 1982; Brown and Zeng, 1994; Patoux, 2004] to incorporate mesoscale to synoptic-scale satellite information into NWP model surface analyses. The high-wavenumber wavelet coefficients of the scatterometer-derived pressure fields were injected into ECMWF SLP analyses over the Southern Ocean with the following method: (1) Swaths of surface pressure were retrieved from QS winds using the UWPBL model. (2) The resulting pressure fields were decomposed using a maximum overlap discrete wavelet transform, which produced a set of two-dimensional wavelet coefficients at scales of 50 km to 1600 km. (3) The ECMWF surface pressure analyses were decomposed using the same wavelet transform. (4) The ECMWF wavelet coefficients at scales less than (and including) 800 km were replaced with the QS-derived wavelet coefficients for swaths occurring within ± 3 hours of the synoptic time. (5) The modified fields were reconstructed by recomposing the wavelet coefficients. As a result, the modified pressure fields contain the large-scale structure of the original ECMWF analyses while also containing the small-scale detail of the QS-derived pressure swaths. Additionally, discontinuities in cyclone tracks that would exist if the tracks were reconstructed from QS pressure swaths alone, owing to gaps between swaths, are eliminated because the gaps now contain ECMWF pressure values and, in particular, cyclone centers if any. When identifying midlatitude cyclone centers and tracks from this new set of pressure fields, more low-pressure centers (5–10% depending on the season), deeper cyclones, and longer tracks were obtained, while the pressure fields contained $\sim 1\%$ additional energy at scales less than 2000 km, and this in spite of the fact that QS winds have been assimilated in the ECMWF NWP model since 22 January 2002. All these features should contribute to the enhancement of momentum and heat fluxes at the air-sea interface.

[7] In order to assess the impact of the injected satellite information inside and outside cyclones, a method was first described for identifying midlatitude cyclones from surface pressure analyses: (1) Local pressure minima over the ocean were first identified in the European Centre for Medium-range Weather Forecasts (ECMWF) surface analyses. (2) If the difference between the central pressure and the surrounding pressure averaged over ± 4 grid points was less than 1 hPa, then the centers were discarded as shallow minima. (3) If the average Laplacian of pressure was less than 0.5×10^{-10} hPa m^{-2} , then the low centers were discarded as weak circulations. The Southern Ocean midlatitude cyclone tracks for the period July 1999 to June 2006 were then reconstructed using the Melbourne University tracking algorithms developed by Murray and Simmonds [1991] and Simmonds *et al.* [1999].

[8] PYL also described a method for estimating the size of a cyclone from the surface pressure field. Following in the steps of previous authors and adapting their schemes, we choose to calculate the distance at which the radial pressure gradient decreases below a certain threshold (2.5×10^{-5} hPa m^{-1}) after going through a maximum. We average that distance over eight radial lines and name it the “radius” of the cyclone, with the understanding that a cyclone is not circular, and that “radius” is another name for “size.” We further estimate the pressure at each of those eight points and average it. We define the “depth” of the cyclone as the difference between that average pressure and the central pressure. The radius is sensitive to the threshold; the particular value of the threshold was chosen subjectively by visual inspection of a large series of cyclones in such a way as to ensure that, in each case, the circle encloses at least all closed isobars, reaches the closest col point, and captures the bulk of the air-sea fluxes in the storm.

[9] We now investigate the impact of the injection of QS information on the estimation of the fluxes inside and outside cyclones. More particularly, we are interested in comparing the role of short-lived mesoscale cyclones with that of longer-lived cyclones. To that effect, we need to: (1) determine the geographical distribution of cyclone tracks as well as the characteristics of the cyclones along those tracks (section 2); (2) estimate the fluxes associated with the cyclones throughout their life cycle (section 3); and (3) integrate the fluxes as a function of storm duration and compare the results for short- and long-lived cyclones (section 4).

2. Cyclone Tracks

[10] In order to understand the impact of midlatitude cyclones on the ocean in terms of air-sea fluxes, it is useful to first establish the geographical context in which those fluxes are taking place, i.e., the geographical distribution of tracks, as well as the areas along those tracks where cyclones are typically deeper, larger, and more intense. Figure 1 shows the cyclone tracks per season and per year for 4 years of the 1999–2006 period, reconstructed from ECMWF analyses with the Melbourne University algorithm. Many of the features described in the recent literature on the Southern Hemisphere, for example, the recent storm track analysis by Hoskins and Hodges [2005], can be observed here. Interseasonal variability can be noted, with a smaller number of tracks in summer (JFM) hugging the coast of the Antarctic

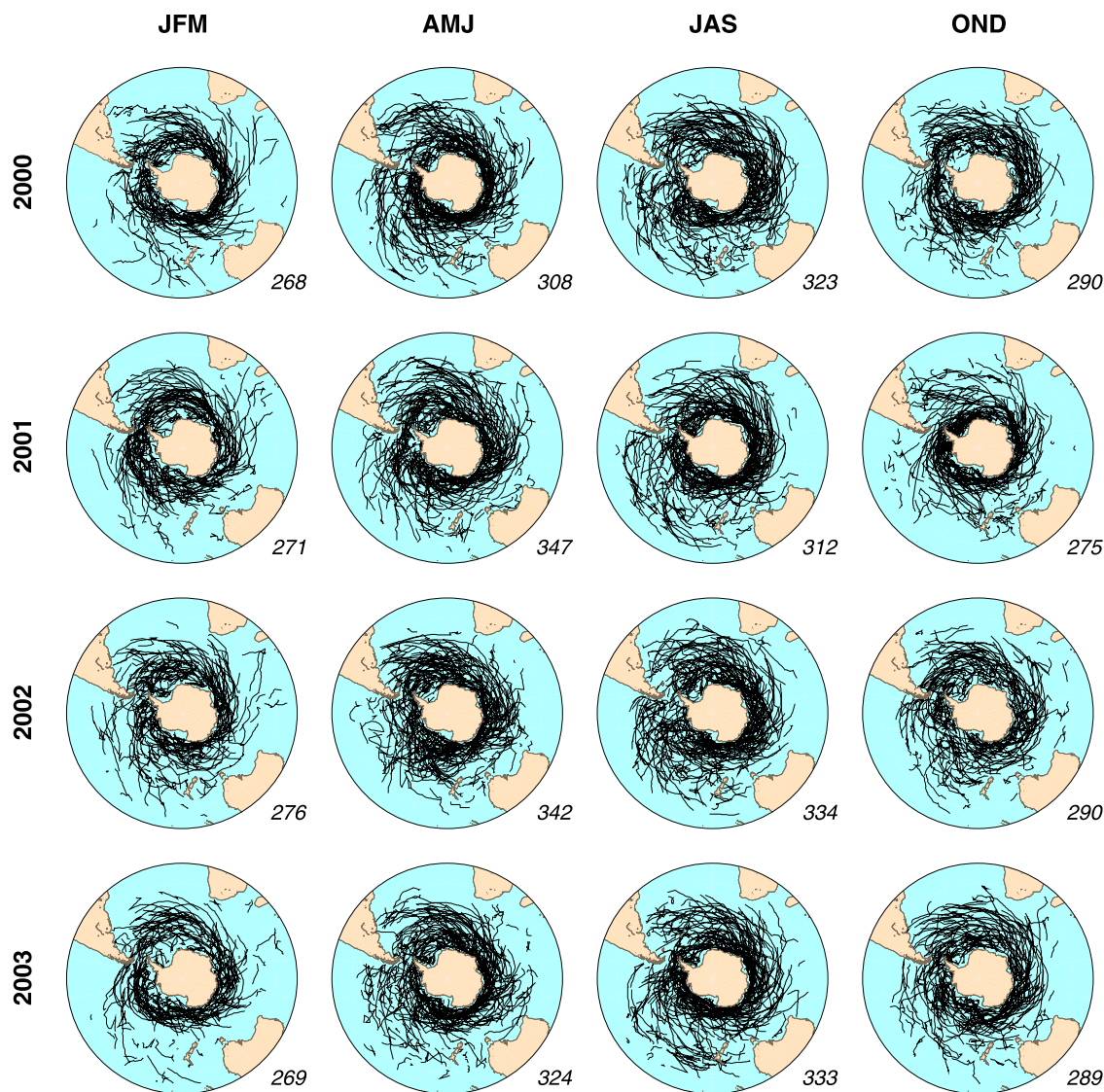


Figure 1. Example of cyclone tracks (2000–2003) calculated from ECMWF surface pressure fields using the University of Melbourne tracking algorithm. The number of tracks is indicated at the bottom right of each plot. Cyclones lasting less than a day are not plotted. Tracks that span two seasons are shown in the plot corresponding to the season in which they spent the most time.

continent at high latitude, and a larger number of tracks in winter (JAS) spanning a broader latitudinal range to the north. The cyclones spiral in southeastward toward Antarctica. A number of tracks originate in the Atlantic Ocean in the lee of the Andes in all seasons and are particularly evident in winter. There is also a larger number of tracks at lower latitude in the Pacific Ocean in winter that is not observed in the other basins and seems to be a specific feature of the Pacific Ocean, as noted by *Hoskins and Hodges* [2005]. Interannual variability can also be observed with, for example, cyclone tracks being more concentrated around the Antarctic continent in JAS and OND 2001 than in other years.

[11] Because these patterns of interseasonal and interannual variability are difficult to analyze from these “spaghetti” plots, various statistics are also computed using the Melbourne University algorithms. These statistics are further averaged over the 7-year study period to produce the seasonal mean results shown in Figures 2, 3, and 4. They are in general

agreement with the results of *Simmonds and Keay* [2000b] based on the 40-year NCEP-NCAR reanalysis. Note in particular the arc of maximum track density hugging the coast of Antarctica from south of the Cape of Good Hope to the Ross Sea, with a higher maximum in autumn and winter (Figure 2a). Midlatitude cyclones initiated east of South America and circling southeastward around the continent are partly responsible for the location of this maximum. The minimum central pressures are also found along the coast of Antarctica (Figure 2c), with a local minimum over the Amundsen Sea. These same locations (Indian Ocean shelf and Amundsen Sea) also correspond to maxima in radius (Figure 3a) and depth (Figure 3c), enhanced in autumn and winter. Finally, Figure 4a reveals enhanced cyclogenesis in the baroclinic zone along the Antarctic coast, where stark temperature contrasts exist between the extremely cold Antarctic sea ice and relatively warmer water [*Simmonds and Murray*, 1999], and where secondary lows often develop

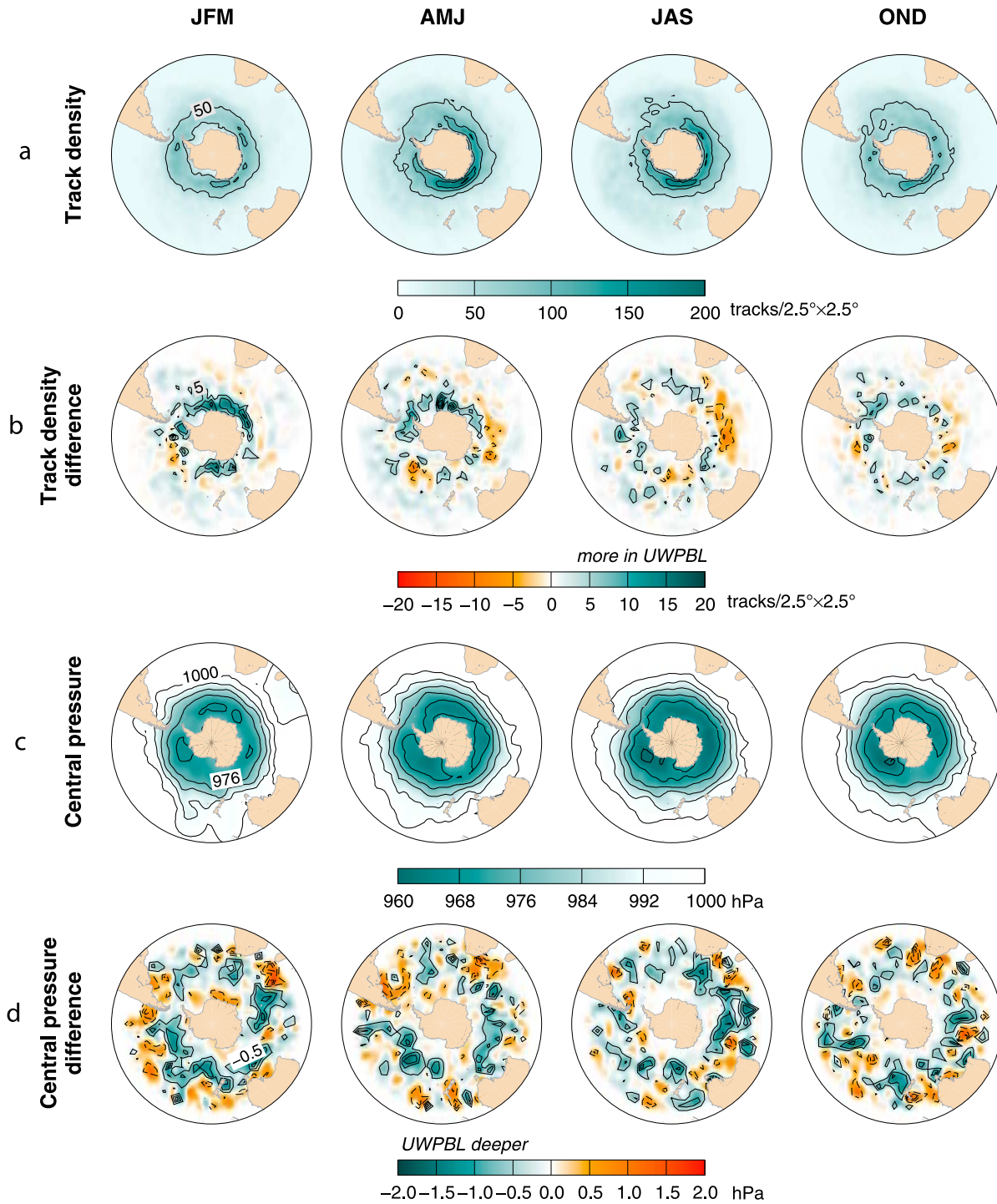


Figure 2. (a) Seasonal mean track density (contour interval 50 tracks/ $2.5 \times 2.5^\circ$). (b) Differences between UWPBL and ECMWF; blue indicates higher track density in UWPBL statistics, solid contours correspond to 3 tracks/ $2.5 \times 2.5^\circ$, while dashed contours have the corresponding negative values. (c) Seasonal mean central pressure (contour interval 8 hPa). (d) Differences between UWPBL and ECMWF; blue indicates deeper central pressure in UWPBL statistics, solid contours correspond to 0.5-hPa central pressure difference, and red and dashed contours have the corresponding negative values.

in the decaying trough of large mature primary cyclones. Note also the area of enhanced cyclogenesis in the lee of the Andes and the Antarctic Peninsula, as well as, to some extent, southeast of Australia and New Zealand. Our climatology does not resolve continental lows and does not capture the

very high latitudes, which removes some regions of intense cyclogenesis, such as the Weddell Sea and the Ross Sea. The region of maximum cyclolysis is concentrated around the Antarctic continent. In autumn and winter, there exists a local cyclolysis maximum off the west coast of Southern Chile,

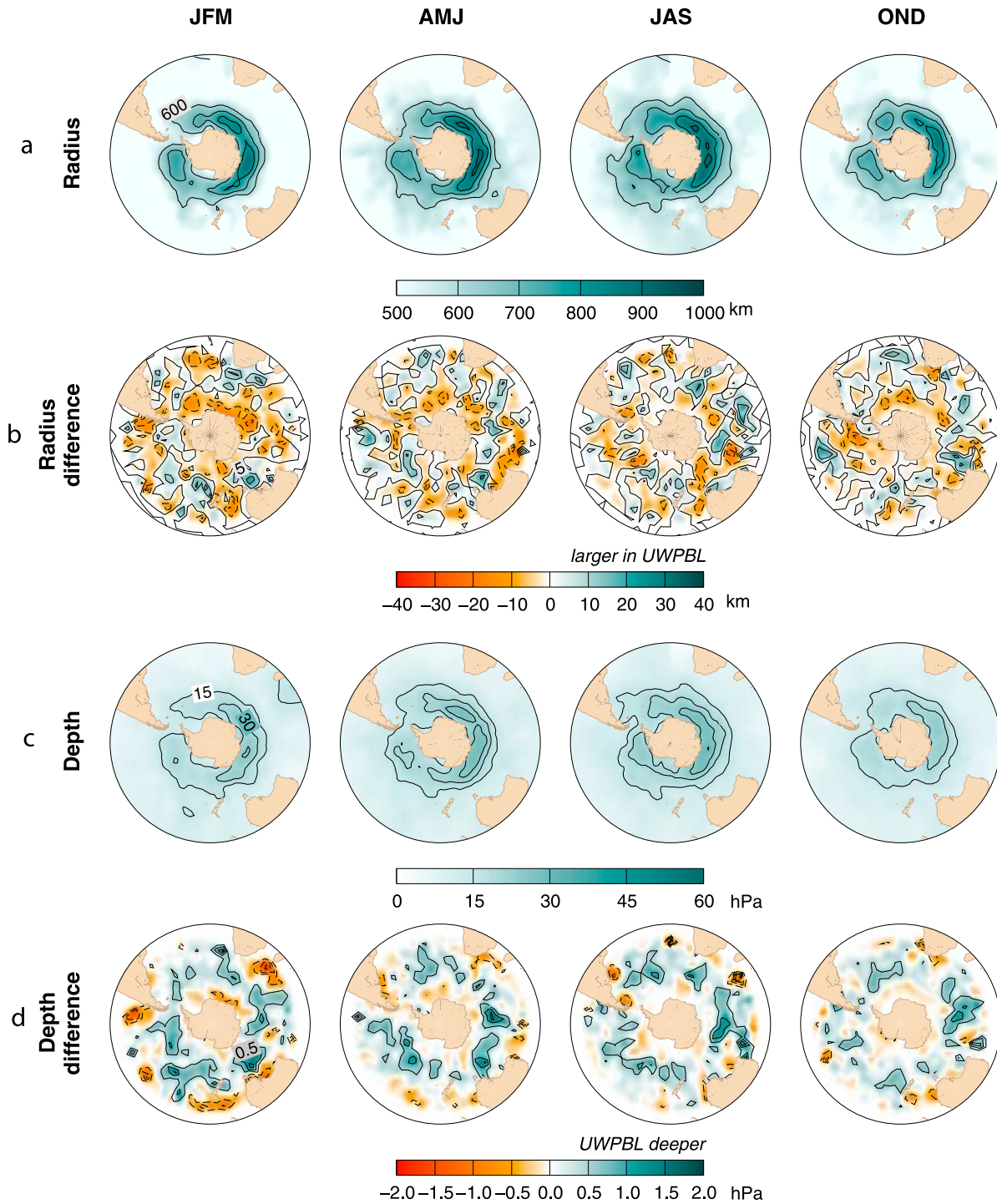


Figure 3. (a) Seasonal mean radius (contour interval 100 km). (b) Differences between UWPBL and ECMWF; blue indicates greater radius in UWPBL statistics, solid contours correspond to 5 km radius difference, while dashed contours have the corresponding negative values. (c) Seasonal mean depth (contour interval 15 hPa). (d) Differences between UWPBL and ECMWF; blue indicates greater depth in UWPBL statistics, solid contours correspond to 0.5-hPa depth difference, and red and dashed contours have the corresponding negative values.

where midlatitude cyclones decrease in intensity by shrinking of the vortex column as they approach the Andes. After crossing the Andes, they are regenerated on the eastern side of the mountain range, as evidenced by the local maximum

in cyclogenesis off the eastern coast of Southern Chile/ Antarctic Peninsula noted above.

[12] Figures 2, 3, and 4 also show the differences between the UWPBL and ECMWF statistics. The differences between

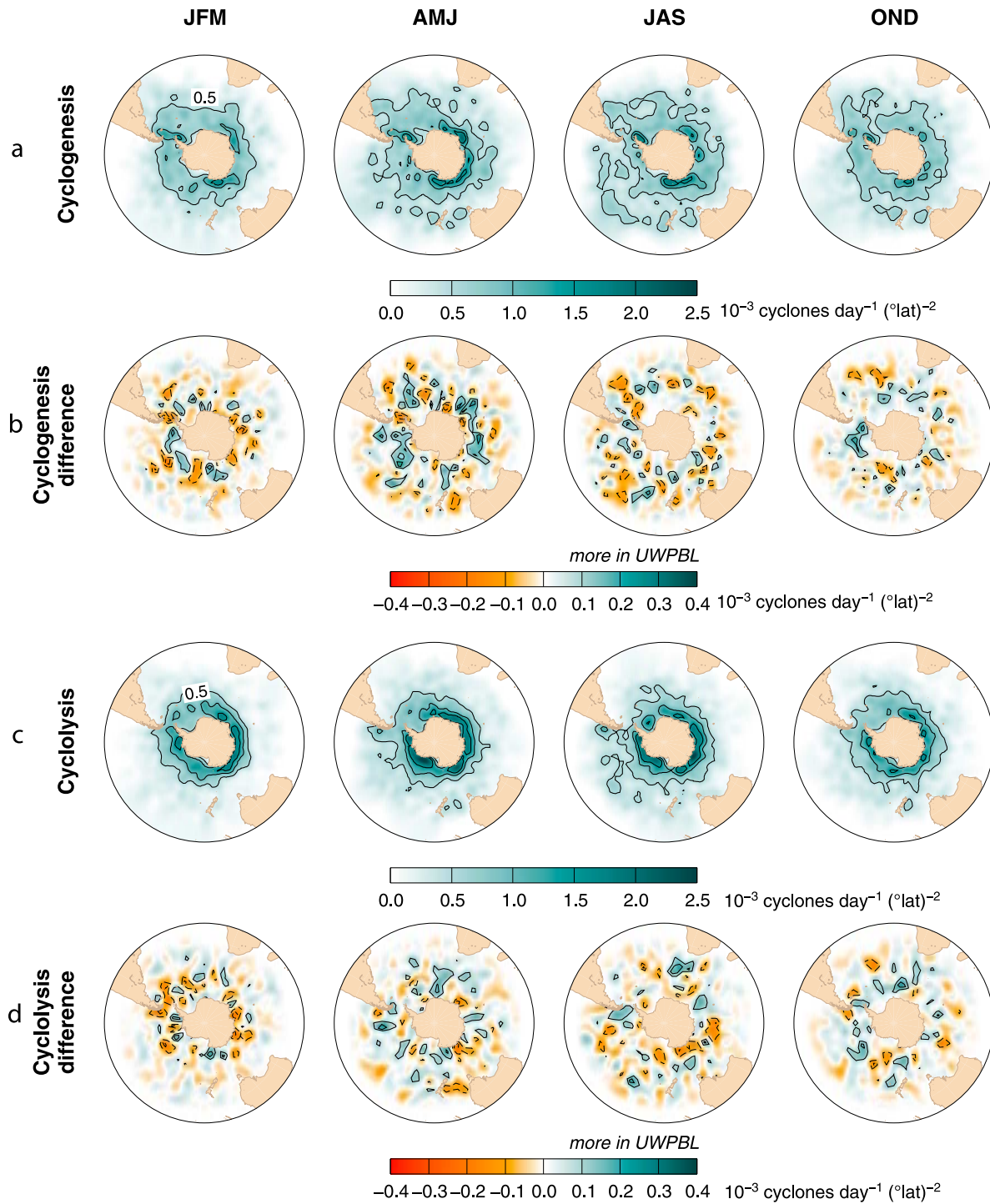


Figure 4. (a) Seasonal mean cyclogenesis (0.5×10^{-3} cyclones $\text{d}^{-1} (\text{°lat})^{-1}$ contours). (c) Seasonal mean cyclolysis (0.5×10^{-3} cyclones $\text{d}^{-1} (\text{°lat})^{-1}$ contours). (b and d) Differences between UWPBL and ECMWF; blue indicates greater occurrence of cyclogenesis and cyclolysis in UWPBL statistics, solid contours correspond to a positive difference of 0.05×10^{-3} cyclones $\text{d}^{-1} (\text{°lat})^{-1}$, and red and dashed contours have the corresponding negative values.

the two data sets are all less than 10%. Figure 2 reveals an overall positive impact of the scatterometer on track density. The impact of the scatterometer-derived pressure swaths is felt closer to the Antarctic continent during the austral summer (when the ice edge retreats toward the continent) and

farther to the north during the austral winter (when no winds are measured by the scatterometer over the ice surrounding Antarctica). Figures 2 and 3 also reveal an overall positive impact on central pressure and depth (in the sense of deeper cyclones), while the impact on the radius is smaller and

slightly negative in the vicinity of the Antarctic continent. Figure 4 shows a slight overall increase in cyclogenesis and cyclolysis in UWPBL relative to ECMWF, consistent with a higher number of tracks in the UWPBL data set. These results are also consistent with the findings of PYL, namely that the impact of the scatterometer is mostly in the form of a higher number of short-lived cyclones, an earlier capture of the incipient stage of cyclones, and a deeper structure (enhanced central pressure and depth with slightly smaller radii).

[13] As suggested by Figure 1, interannual variability exists with all variables, but no trend could be detected with this relatively short 7-year record. The individual plots showing the seasonal means per year for all variables are therefore not shown.

3. Surface Fluxes

[14] With the geographical distribution of midlatitude cyclone tracks in mind, as well as the areas of most dense and most intense cyclonic activity, we now proceed to estimating the associated air-sea fluxes (inside cyclones) and comparing them to the fluxes over the rest of the ocean. First, the methodology for calculating the fluxes is described. It is then applied to individual storms at each stage of their life cycle. The time evolution of the spatial integrals is analyzed inside and outside cyclones. Finally, the spatial integrals for short-lived versus long-lived cyclones are presented in section 4.

3.1. Methodology

[15] The surface fluxes are calculated using a planetary boundary layer (PBL) model in which the SLP, the sea-surface temperature (T_s), and the surface air temperature (T_a) are inputs to the model. T_s and T_a are obtained from ECMWF. The SLP is either the ECMWF surface analysis, or the same analysis modified with the scatterometer information as described by PYL. We used the University of Washington PBL model [Brown and Levy, 1986; Brown and Liu, 1982; Brown and Zeng, 1994; Patoux, 2004] with modifications following the 2003 updates to the Coupled Ocean-Atmosphere Response Experiment (COARE) parameterizations (COARE 3.0). These updates are described in detail by Fairall *et al.* [2003] and in the online documentation at ftp://ftp.etl.noaa.gov/user/cfairall/bulka/g/cor3_0/ and will only be summarized here.

[16] The momentum flux (i.e., the stress magnitude, referred to simply as the stress in the rest of the article), the fluxes of sensible heat, and latent heat respectively are defined as

$$\tau = \rho u_*^2, \quad (1)$$

$$H = C_p \rho u_* T_*, \quad (2)$$

$$Q = L_v \rho u_* q_*, \quad (3)$$

where ρ is the air density, C_p is the specific heat capacity of air, L_v is the latent heat of vaporization, and T_* , q_* , and the friction velocity u_* are characteristic scales for temperature,

humidity, and wind speed respectively, at the air-sea interface. They are determined, along with the roughness lengths z_0 , z_{0T} , and z_{0q} , by iteration on the logarithmic profiles,

$$u_* = \frac{k\Delta U}{\ln(10/z_0)} - \Psi_u, \quad (4)$$

$$T_* = -\frac{k\Delta T}{\ln(10/z_{0T})} - \Psi_T, \quad (5)$$

$$q_* = -\frac{k\Delta q}{\ln(10/z_{0q})} - \Psi_q, \quad (6)$$

and a modified Charnock formula,

$$z_0 = \alpha \frac{u_*^2}{g} + 0.11 \frac{\nu}{u_*}, \quad (7)$$

where the so-called Charnock parameter is defined as

$$\begin{aligned} \alpha &= 0.011 \quad \text{if } \Delta U < 10 \text{ m s}^{-1}, \\ \alpha &= 0.011 + (0.018 - 0.011) \frac{\Delta U - 10}{18 - 10}, \\ &\quad \text{if } 10 < \Delta U < 18 \text{ m s}^{-1}, \\ \alpha &= 0.018 \quad \text{if } 18 < \Delta U. \end{aligned} \quad (8)$$

The roughness lengths z_{0T} and z_{0q} are obtained with a modification of the Liu-Katsaros-Businger (LKB) parameterization [Liu *et al.*, 1979],

$$z_{0T} = z_{0q} = \min(1.15 \times 10^{-4}, 5.5 \times 10^{-5}/R_r^{0.6}). \quad (9)$$

In the above equations, ΔU , ΔT , and Δq are the differences in wind speed, temperature and humidity respectively between 10 m and the ocean surface, while Ψ_u , Ψ_T , and Ψ_q are stratification corrections calculated at 10 m height (see the COARE documentation for the exact formulation), g is the standard acceleration of gravity, ν is the kinematic viscosity of air, and R_r is the roughness Reynolds number $R_r = z_0 u_* / \nu$. ΔU is further modified to account for subgrid-scale wind gusts by adding a gustiness factor W_g such that

$$\Delta U = \sqrt{U_{10}^2 + W_g^2}, \quad (10)$$

$$\begin{aligned} W_g &= 1.25 (B_f z_i)^{1/3} \quad \text{if } B_f > 0, \\ W_g &= 0.2 \quad \text{if } B_f < 0, \end{aligned} \quad (11)$$

$$B_f = -\frac{g}{T_a} u_* (T_* + 0.61 T_a q_*), \quad (12)$$

where U_{10} is the wind speed at 10 m height.

[17] The fluxes are calculated at each grid point (over the ocean) and then integrated spatially over the size of each in-

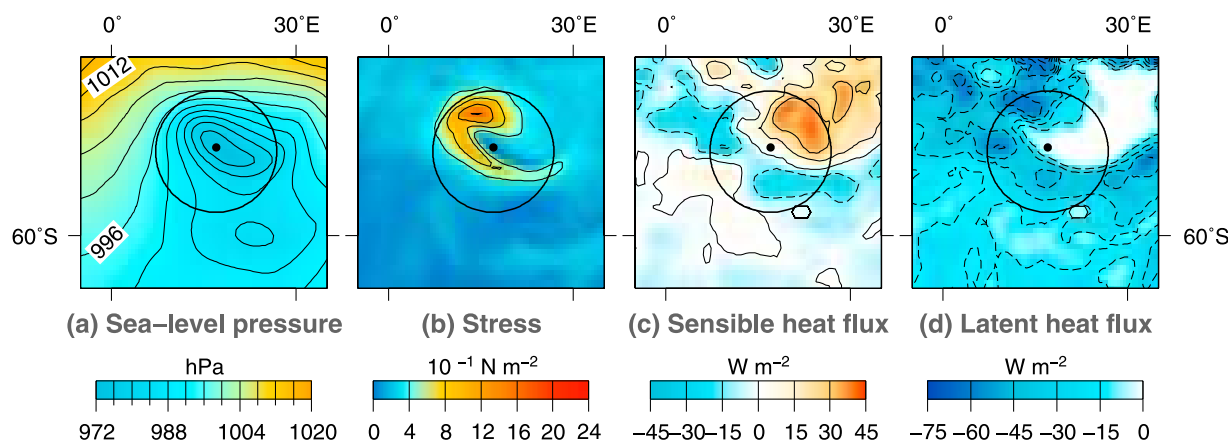


Figure 5. Example of the calculation of fluxes associated with a cyclone, 5 January 2003, 1200 UTC. The minimum pressure location is indicated with a black dot. The size of the cyclone is indicated with a circle. (a) The contours are 4-hPa isobars. (b) The contour interval is 0.4 N m^{-2} . (c, d) Solid lines are positive contours, dashed lines are negative contours, and bold lines are zero contours.

dividual cyclone. An example is shown in Figure 5. Figure 5a shows the SLP field corresponding to a Southern Ocean cyclone on 5 January 2003 south of the Cape of Good Hope, at an intermediate stage of its development. The storm center (pressure minimum) is indicated by a black dot while the storm extent is delineated by a circle (see PYL). Note that the circle almost fully encloses the outermost closed isobar. A cold front extends northeast of the storm, as suggested by the kinks in the isobars. Figures 5b, 5c, and 5d show the fluxes of momentum and heat calculated as described above. The details of the flux fields are not so important as their general structure with respect to the storm center and shape. The stress is maximum on the northwest flank of the storm, where the isobars are the tightest, and the area of maximum stress wraps around the storm center, following the general direction of the front. The stress decreases rapidly away from the area of strongest winds, and the circle approximating the extent of the cyclone therefore captures most of it. The sensible heat flux is positive on the northeastern half of the cyclone (warm air advection over cooler water: the ocean gains heat) as indicated by the solid contours, and negative on the southwestern half of the cyclone (cold air advection from Antarctica over relatively warmer water: the ocean loses heat) as indicated by the dashed contours and summarized schematically in Figure 6. Arguably, the circle approximating the extent of the cyclone is less successful at capturing all the heat exchanges associated with the cyclone than it is at representing stress. One can observe positive and negative fluxes outside of the circle that can be considered part of the cyclonic system. However, the circle more or less captures the areas of “maximum” fluxes and constitutes a fairly good approximation. Slight changes in the threshold characterization increase or decrease the total fluxes, but do not significantly impact the qualitative results presented below. A similar observation is made with the latent heat flux. Note that the latent heat fluxes are larger in magnitude than the sensible heat fluxes and are the main source of heat loss by the ocean, as will be seen in the following section.

3.2. Storm Life Cycle

[18] The time evolution of the surface fluxes during an extratropical cyclone life cycle is now illustrated with the

example of an 8-day cyclone appearing in the lee of the Andes and traveling eastward to the Cape of Good Hope, then veering southeastward toward Antarctica on 8–15 June 2005 (Figure 7). The central pressure of the cyclone gradually decreases until day 4 when it starts to drop quickly until day 6. The depth and radius of the storm reach their maximum on day 7. The modified pressure fields suggest slightly deeper lows along the track except in three instances. They also suggest a longer track, extended by one synoptic period at the beginning and two periods at the end. The corresponding flux integrals are shown in Figure 8. The spatial integral in Figure 8 (left) provides a quantitative estimate of the contribution of the storm to the fluxes of momentum and heat into the ocean. By dividing the contributions by the area of the storm (Figure 8, right), one obtains an estimate of the average intensity of the fluxes inside the storm at each step of the storm life cycle. For example, in Figure 8a, the integrated

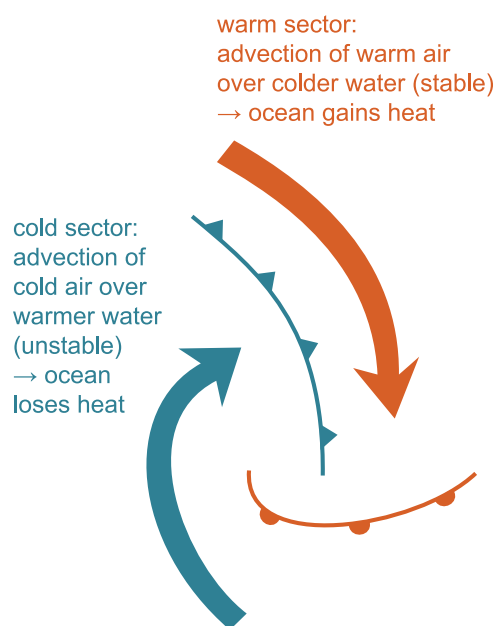


Figure 6. Idealized Southern Ocean midlatitude cyclone.

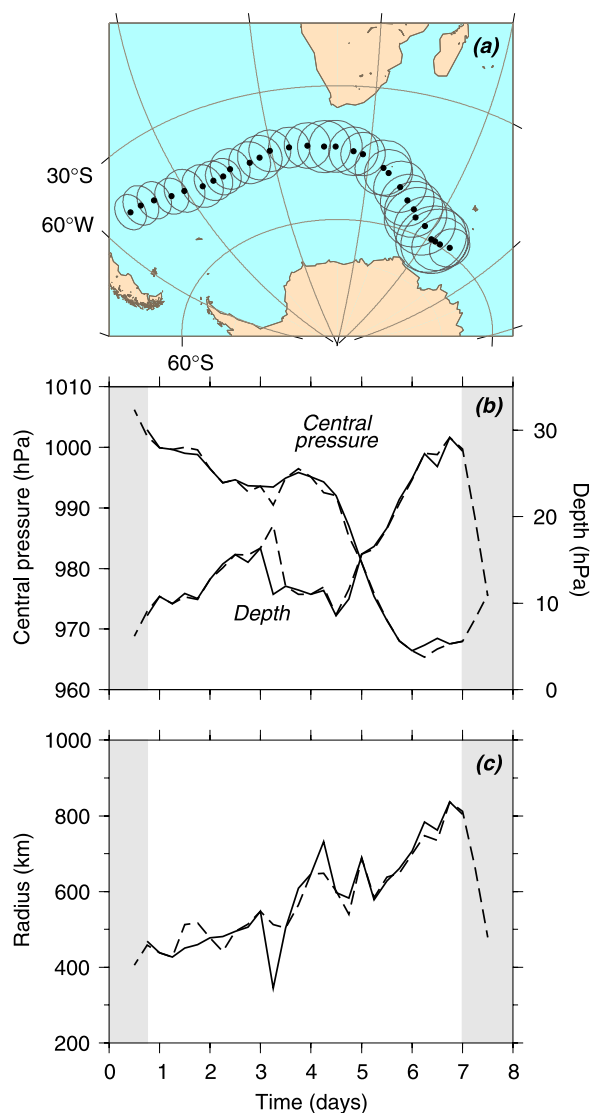


Figure 7. (a) Path of cyclone south of Africa on 8–15 June 2005. Comparison of (b) the central pressure and depth and (c) radius of a cyclone. Solid lines show values calculated from the ECMWF database while dashed lines correspond to the UWPBL database. Gray shading in Figures 7b and 7c indicates the synoptic periods when the storm position is captured only in the UWPBL pressure fields.

stress is largest toward the end of the life cycle because the storm extent is the greatest then. But after dividing by the area (Figure 8b), we see that the average stress is smaller at the end than, for example, around day 3.

[19] The sensible heat gained by the ocean under the warm sector of the cyclone is maximum on day 6, while the sensible and latent heat loss under the cold sector is maximum on day 5 (Figures 8c and 8g; see also Figure 6). After dividing by the area, we see that, except for the sensible heat gain, the fluxes tend to be maximum around days 3 and 4, and decrease significantly afterward. This decrease is partly due to the fact that, when the cyclone reaches its mature stage, the distribution of fluxes is uneven inside the circle approximating the shape of the cyclone. There exist regions of maximum intensity (such as along the advection of cold and warm air) while

large regions within the circle contain no significant fluxes (and decrease the average).

[20] Figure 8 also compares the fluxes calculated with the ECMWF SLP analyses (solid lines) with the fluxes calculated with the UWPBL pressure fields (dashed lines). While they follow the same evolution overall, the UWPBL fluxes are slightly different, both in spatial integral and spatial average, with a tendency for stronger fluxes in the UWPBL case. Note that these differences can have several origins: the scatterometer might be capturing meteorological features that are neither modeled nor assimilated in the NWP model; the scatterometer measures the wind relative to the moving ocean, while the ECMWF winds are relative to a stationary surface [Kelly *et al.*, 2001]; there are instrumental errors, wind retrieval errors due to the sampling geometry of the scatterometer antenna, and random errors in the retrieval of QS winds that can translate into errors in the flux calculation. However, because all those factors are channeled through the retrieval of individual pressure swaths, the wavelet decomposition, the injection of wavelet coefficients into the ECMWF pressure fields, the repositioning of the pressure fields, and the calculation of the fluxes via a PBL model, it is quite difficult to disentangle them and ascertain the predominance of one factor over another. White noise experiments in which the impact of randomly distributed errors on the pressure retrieval was estimated by injecting white noise in individual swaths of QS winds have shown a limited impact on the pressure fields (not shown). One could therefore assume that a positive or negative difference observed in the fluxes averaged over time and space could be assigned to the other factors. This can be investigated in two ways. (1) By summing the contributions of all cyclones at a given synoptic time, we can construct a time series of hemispheric fluxes inside cyclones and over the entire Southern Ocean. (2) By sorting the cyclones by life span, we can investigate the exchanges of momentum and heat between the Southern Ocean and short-lived depressions (mesoscale cyclones) as opposed to long-lived extratropical cyclones. Each of these calculations is now presented.

3.3. Hemispheric Fluxes

[21] The time evolution of the spatially integrated fluxes is presented in Figures 9a, 9c, and 9e where the integral is performed at each synoptic time over the area contained within extratropical cyclones on one hand and the entire Southern Ocean under all weather on the other hand. Here the Southern Ocean is defined as the body of water contained between 80°S and 20°S. The average fluxes are obtained by dividing the spatial integral by the area of the storms and by the area of the entire Southern Ocean, respectively (Figures 9b, 9d, and 9f). Because the daily variability in the distribution of synoptic systems, both in shape and intensity, is large, the time series present a high-frequency component (background gray lines) modulated by the seasonal cycle. For readability, all the time series presented hereafter are filtered with a traditional Lanczos filter at 90-day cutoff (solid and dashed black lines). This removes the intraseasonal variability and highlights the interannual variability.

[22] The spatially integrated momentum flux taking place within the storms represents about 25% of the total flux into the ocean (Figure 9a). However, Figure 9b shows that the average stress within cyclones is about twice as large as over

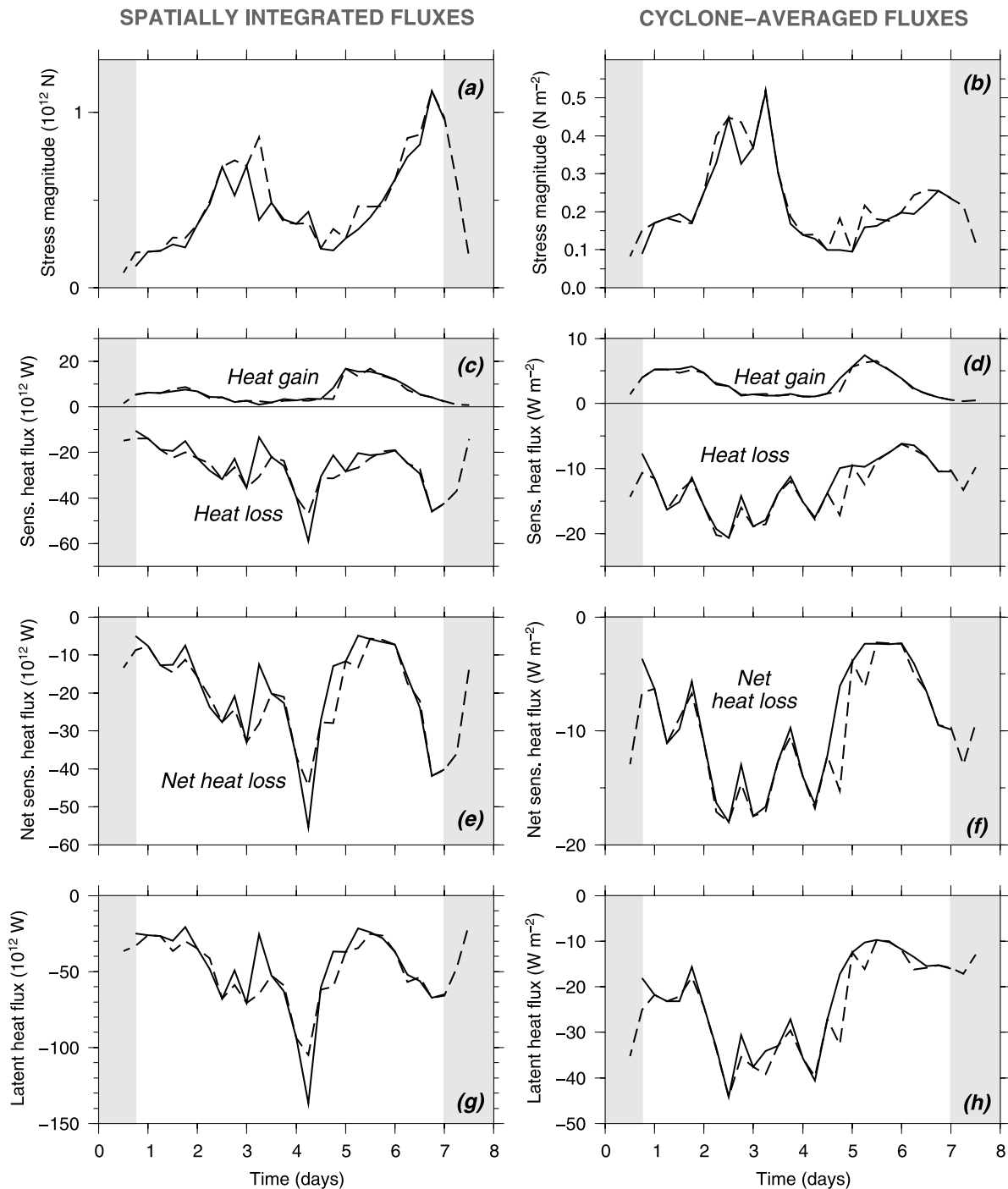


Figure 8. Comparison of fluxes (left) spatially integrated and (right) averaged over the area of the cyclone, 8–15 June 2005. Solid (dashed) lines show fluxes calculated from the ECMWF (UWPBL) database. Gray shading indicates the synoptic periods when the storm position is captured only in the UWPBL pressure fields.

the entire ocean. Midlatitude cyclones are characterized by stronger surface winds and therefore a stronger momentum flux (a square of the wind speed). However, because the area covered by the storms is much smaller than the entire ocean, the spatial integral of the momentum flux within storms is also smaller than the integral over the entire ocean.

[23] The sensible heat lost within cyclones is only about 15% of the total sensible heat lost by the entire Southern

Ocean under all weather conditions (Figure 9c). Within a midlatitude cyclone, sensible heat is lost by the ocean in the cold sector, but there is also a sensible heat gain in the warm sector (see Figure 6). The net loss is therefore smaller than over the rest of the ocean, where the sea-surface temperature is on average higher than the surface air temperature [Peixoto and Oort, 1992]. Figure 9d shows that the seasonal amplitude of the average sensible heat flux is larger within cyclones than

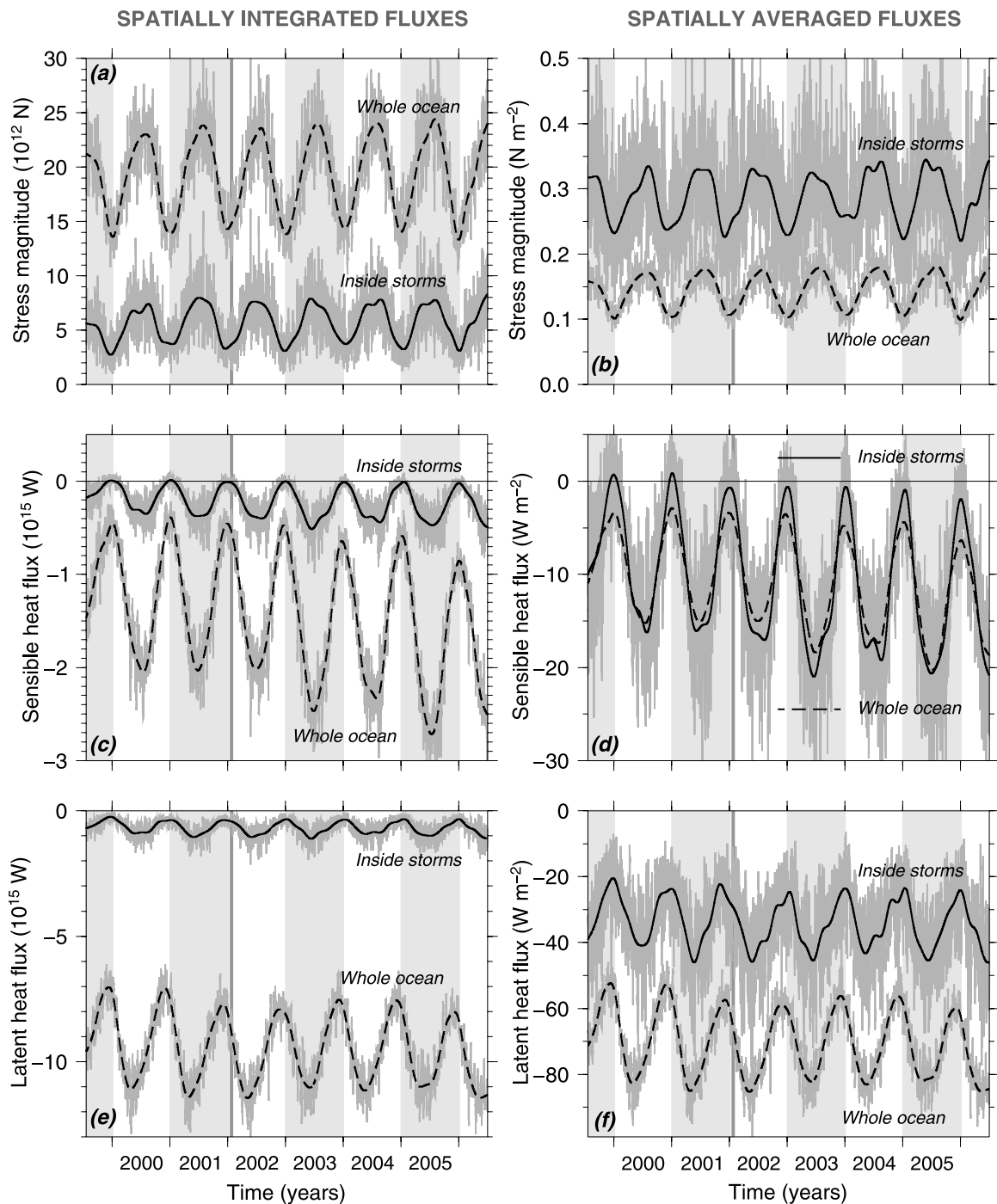


Figure 9. Time evolution of fluxes (in gray) (left) spatially integrated over the area of the cyclones and over the ocean and (right) averaged over the interior and exterior of the cyclones, July 1999 to June 2006, from ECMWF. The solid lines are 90-day running means of the gray lines. Years are indicated in the background with alternating bands of gray. The vertical gray line indicates 22 January 2002, when ECMWF started assimilating QS winds.

for the entire ocean. In winter, the heat loss is larger within cyclones, where the advection of cold air from the Antarctic continent covers extended areas where the winds are relatively strong, resulting in strong upward sensible heat fluxes. In summer, the net sensible heat flux is about zero, showing that there is an approximate balance between the heat gained and lost in the warm and cold sectors, respectively.

[24] The latent heat loss within cyclones is less than 10% of the total latent heat lost by the ocean (Figure 9e). A mid-latitude cyclone is a region where the humidity is relatively high, which does not favor evaporation. Over the rest of the ocean, however, and especially in regions where dry cold air from the Antarctic continent sweeps over the warmer waters of the Southern Ocean, the vertical humidity gradient, and

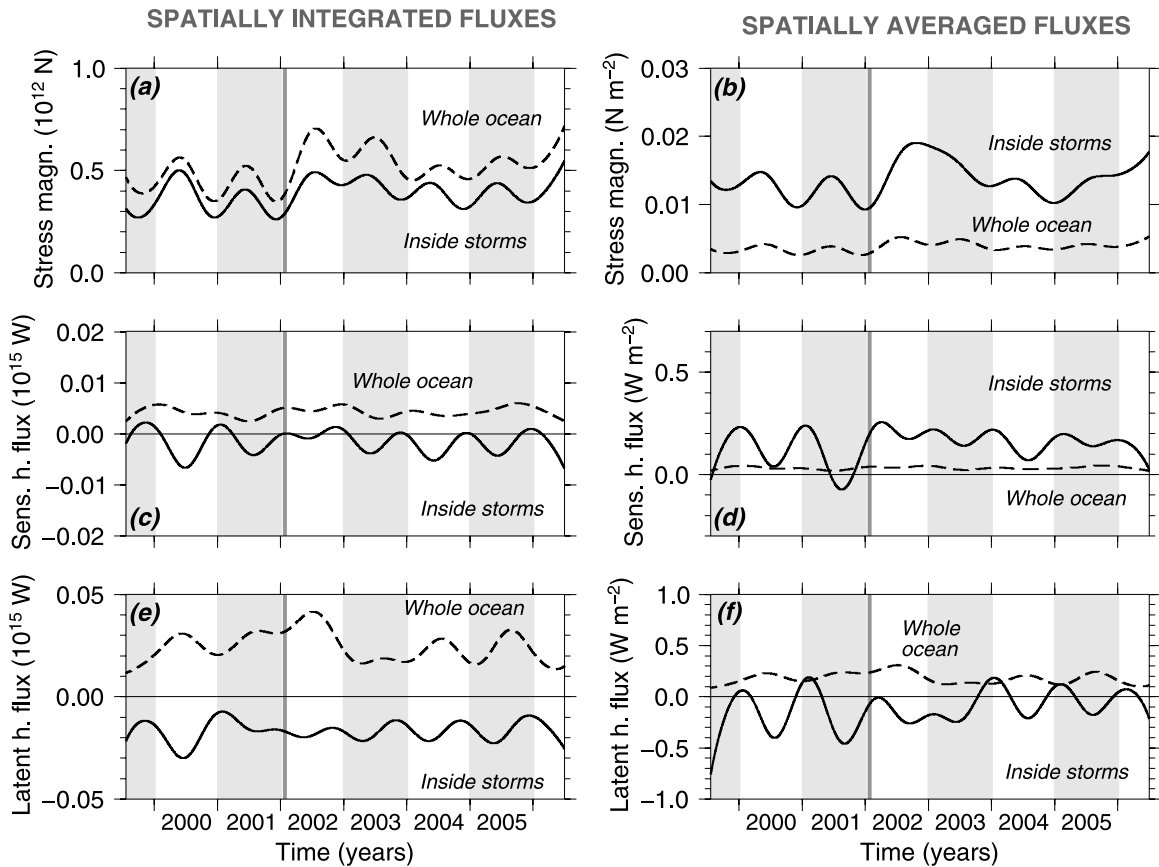


Figure 10. Differences between UWPBL and ECMWF fluxes, Same coding as Figure 9.

therefore the evaporative flux, is larger. This is confirmed in Figure 9f, where the average latent heat flux is about twice as large over the ocean as it is within cyclones.

[25] Finally, we compare the flux climatology obtained with ECMWF surface pressure analyses with the UWPBL climatology obtained after injection of QS information into the analyses. The results are presented in Figure 10, where the differences calculated at each synoptic time have been Lanczos-filtered (because the difference is noisier, we have filtered the time series at a 360-day cutoff to reveal the inter-annual variability). The momentum flux is slightly stronger after injection of QS information (i.e., the difference is positive in panels a and b), while the differences for the sensible and latent heat fluxes differ within and outside of midlatitude cyclones. The results are averaged and summarized in Table 1. Note, however, that only the differences in stress (both spatially integrated and spatially averaged) and the differences in spatially averaged latent heat flux are statistically significant at the 95% level (in the mean of the unfiltered time series).

[26] There is little interannual variability over the 7 years of results plotted in Figure 9. Of interest, however, is an apparent increase in the fluxes in the second half of the record. Before considering geophysical changes such as a climatic trend, we must first consider possible changes in the data. A possible explanation is the change in SST representation from Reynolds SST to Real-Time Global (RTG) SST effected by ECMWF in May 2001. A more accurate depiction of the thermal stratification over the ocean might have resulted in stronger sensible heat fluxes overall. The horizontal and

vertical grid resolution of the ECMWF NWP model was also changed in November 2000, which could have improved the representation of mesoscale atmospheric structures along with the associated fluxes. Another possible explanation is the assimilation of QS winds by ECMWF starting 22 January 2002 (the date is indicated in all panels of Figure 9 with a vertical gray line). Stronger surface winds might result in stronger sensible heat fluxes. In this case, the agreement between the two data sets should improve in Figure 10 after assimilation of QS winds by ECMWF. However, the differences between

Table 1. Summary of the Differences in Flux Magnitude Between ECMWF and UWPBL Data Sets^a

Flux Type	UWPBL % Greater Than ECMWF
<i>Spatially Integrated</i>	
Stress magnitude (cyclones)	+7.8
Stress magnitude (Southern Ocean)	+2.1
Sensible heat loss (cyclones)	+1.5
Sensible heat loss (Southern Ocean)	-0.3
Latent heat loss (cyclones)	+2.9
Latent heat loss (Southern Ocean)	-0.3
<i>Spatially Averaged</i>	
Stress magnitude (cyclones)	+4.6
Stress magnitude (Southern Ocean)	+3.1
Sensible heat loss (cyclones)	-1
Sensible heat loss (Southern Ocean)	-0.3
Latent heat loss (cyclones)	+0.3
Latent heat loss (Southern Ocean)	-0.3

^aItalics indicate that the difference is not statistically significant.

ECMWF and UWPBL momentum fluxes are in fact larger after the beginning of QS assimilation by ECMWF. Note that the difference between the mean of the fluxes before 22 January 2002 and the mean of the fluxes afterward is statistically significant at the 95% level for momentum, sensible and latent heat. However, because ECMWF updates its model regularly, it can be difficult to disentangle the effects of the various changes and it is impossible to assign the observed difference to the assimilation of QS winds exclusively (a detailed list of the changes can be found at http://www.ecmwf.int/products/data/operational_system/evolution). These results remain unclear and will require further investigation.

4. Mesoscale Cyclones Versus Large Storms

[27] The abundance of mesoscale cyclones, or subsynoptic-scale low-pressure systems, is a unique feature of the mid-latitudes to high southern latitudes, particularly in the polar region south of the polar front, where intense mesoscale cyclones with gale force wind speeds are often observed (polar lows). Because of their small spatial scale and short life span, these mesoscale cyclones are not easy to document over the data-sparse Southern Ocean and are not well represented in numerical models. However, they have been investigated extensively since satellite observations, such as Advanced Very High Resolution Radiometer (AVHRR) and microwave measurements, have become available in the last 40 years [Carleton and Carpenter, 1990; Fitch and Carleton, 1992; Carleton, 1995; McMurdie et al., 1997; Marshall and Turner, 1997; Carleton and Song, 1997; Rasmussen and Turner, 2003]. Condron et al. [2006] recently showed that the number of Northeast Atlantic cyclones less than 500 km in size was underestimated in the 40-year ECMWF reanalysis data set as compared to cloud vortices detected in satellite imagery, which may affect the estimation of the associated air-sea fluxes. Here we are interested in the exchange of momentum and heat between the atmosphere and the ocean associated with mesoscale cyclones over Southern Ocean.

[28] While previous studies have classified mesoscale cyclones on the basis of their size or cloud signature, we chose here to sort them by life span and to investigate the role played by “short-lived” cyclones (here defined as lasting less than 4 days) as opposed to “long-lived” large cyclones (lasting 4 days or longer). Among all “short-lived” cyclones, we chose those well-established mesoscale cyclones that appear over at least four time steps (24 hours). These mesoscale cyclones include polar lows with strong winds as well as less intense low-pressure centers. Figure 11 shows that beyond 4 days, the average central pressure, radius, and depth remain relatively constant. While the choice of a 4-day threshold might seem arbitrary, it is consistent with previous definitions based on size (e.g., 200–1000 km [Rasmussen and Turner, 2003; Blechschmidt, 2008]), as well with the conventional wisdom that mesoscale cyclones often last 3 to 4 days. It also has the advantage of separating cyclones in two distinct ranges of the central pressure, radius, and depth distributions. It is also noted in Figure 11 that the mean central pressure sharply drops, and radius and depth rapidly increase for cyclones lasting longer than 12 days. These likely represent “super storms,” which are also an interesting subject. However, since our focus is on the flux contribution

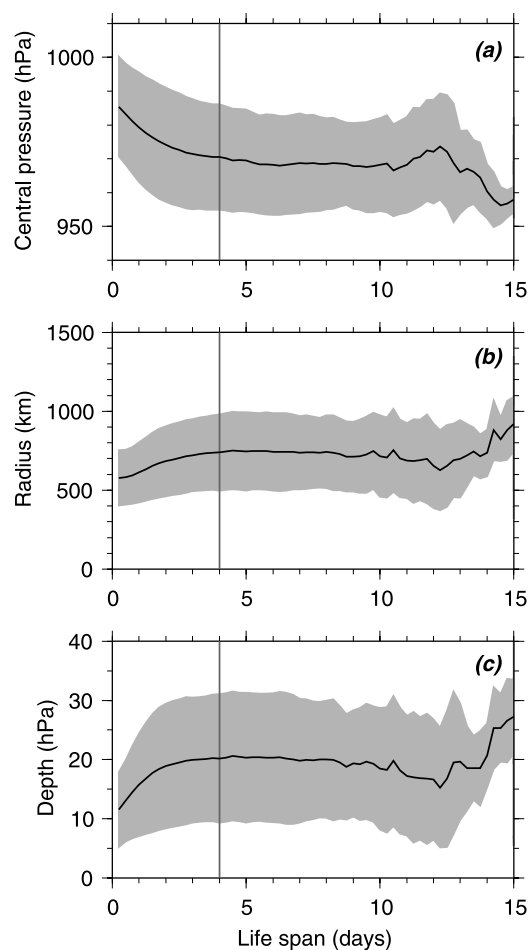


Figure 11. Mean (solid line) and standard deviation (gray shading) of the (a) central pressure, (b) radius, and (c) depth of Southern Ocean midlatitude cyclones. The vertical line indicates the 4-day threshold.

from mesoscale cyclones versus large storms, here we do not differentiate the super storms from the other large storms.

[29] Figure 12 shows that the short-lived midlatitude cyclones so defined account for about 75% of all tracks and about 60% of all storm center positions, with little interannual variability. Figure 13 reveals a stronger contrast between the regions of cyclogenesis (Figure 13d) and the regions of cyclolysis (Figure 13e) for large cyclones, which can form in the midlatitudes to high latitudes but usually die at high latitude over the Antarctic polar seas. Figure 13f therefore shows net cyclogenesis in the midlatitudes and net cyclolysis in the polar seas for large cyclones. On the other hand, cyclogenesis and cyclolysis are more evenly distributed for mesoscale cyclones. Note that there is more mesoscale cyclone activity over the polar waters than in the midlatitudes. In both cases, consistent with Figure 4, there is a clear maximum in cyclogenesis southwest of Argentina and the Cape of Good Hope (Figures 13c and 13f). Note also the cyclogenesis/lysis dipoles straddling the Andes, the Antarctic Peninsula, southeast Australia, and New Zealand, highlighting the regions of enhanced cyclogenesis and cyclolysis described earlier (Figure 13c).

[30] Figure 14 shows that, while the flux contribution of short-lived and long-lived cyclones is overall similar, long-lived

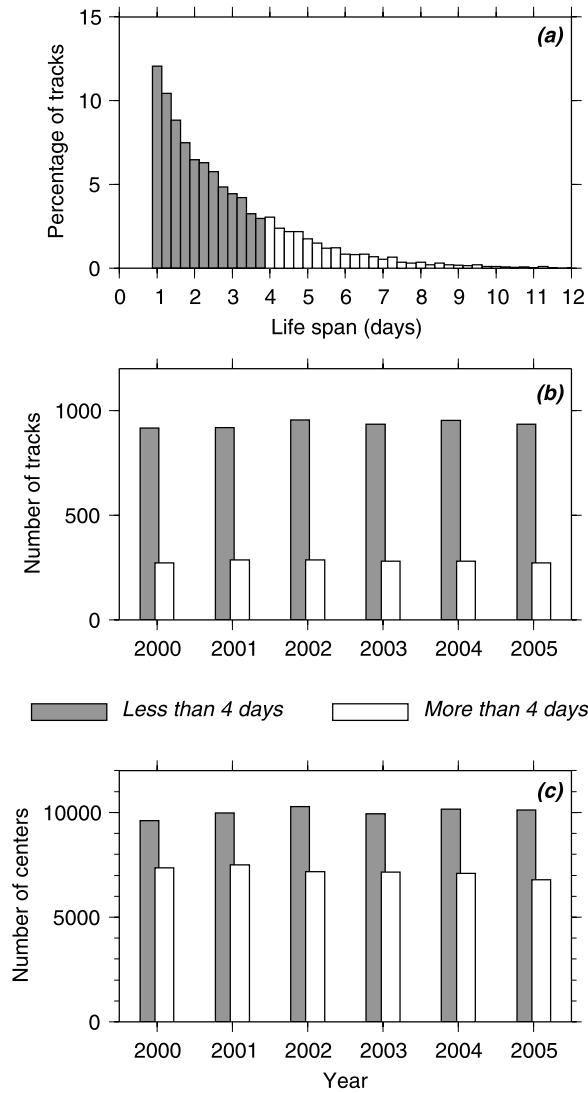


Figure 12. (a) Frequency distribution of midlatitude cyclone tracks as a function of life span. Comparison of (b) the number of tracks and (c) the number of cyclone positions corresponding to short-lived versus long-lived midlatitude cyclones.

cyclones impart slightly more stress and remove slightly more heat than short-lived cyclones in specific areas, such as along the Indian Ocean shelf (about 40% more stress, 30% more sensible heat, and 40% more latent heat) and over the Amundsen Sea (20% more stress, 40% more sensible and latent heat). Even though they are much fewer in number, the combination of a longer life span, a larger size, and most likely stronger winds throughout the cyclone, yields a flux contribution of equal or larger magnitude than the contribution of short-lived cyclones. Note however that the short-lived cyclone fluxes are comparatively more evenly distributed with, for example, a larger contribution over the Pacific Ocean. It is also evident that the ocean loses more sensible heat at high latitude than in the midlatitudes while latent heat fluxes are more evenly distributed from midlatitudes to high latitudes for both types of cyclones. Figure 14 was generated by averaging the winter statistics over the 2000–2005 period.

Although smaller in magnitude, the statistics calculated for the other seasons reveal similar features (not shown).

5. Impact of Parameterizations

[31] The previous analysis should be punctuated by a word of caution. There exist numerous flux products with various parameterizations. The lack of in situ measurements over the Southern Ocean makes it difficult to validate any of these products, leaving us with no better option than comparing the products with each other. *Kubota et al.* [2003] perform such a comparison between five latent heat flux products and find significant differences due in part to a lack of observations in certain regions of the World Ocean and to differences in the surface wind used to calculate the fluxes. *Rouault et al.* [2003] suggest that an underestimation of surface heat fluxes in NWP analyses may occur because their SST representation does not adequately resolve oceanic mesoscale variability that can contribute to large values of air-sea temperature difference. In this article we have concentrated on the impact of scatterometer information on the integrated exchange of momentum and heat between the atmosphere and the ocean. Therefore, the differences between the fluxes with and without the scatterometer information have been our focus over differences between flux products. The same analysis performed with three other flux parameterizations yielded the same qualitative results (e.g., larger stress when incorporating scatterometer information; not shown). However, the differences between the various parameterizations themselves can be as large or greater than the differences we have observed after incorporating scatterometer-derived pressure fields. To illustrate this point, we now show the spatial integration performed with three different flux calculations: (1) the ECMWF fluxes provided as part of the analysis products (ds111.3 files obtained from NCAR); (2) the fluxes calculated with the coefficients developed by Mark Bourassa at Florida State University [Bourassa, 2006]; and (3) the fluxes calculated with standard bulk coefficients and ECMWF surface fields as follows:

$$\tau = \rho C_d U_{10}^2, \quad (13)$$

$$H = \rho C_p C_h U_{10} (T_a - T_s), \quad (14)$$

$$Q = \rho L_v C_l U_{10} (q_a - q_s), \quad (15)$$

where $C_d = 1.2 \times 10^{-3}$ if $U_{10} \leq 11 \text{ m s}^{-1}$ and $C_d = (0.49 + 0.065 U_{10}) \times 10^{-3}$ if $U_{10} > 11 \text{ m s}^{-1}$, $C_p = 1005 \text{ J kg}^{-1} \text{ K}^{-1}$, $C_h = C_l = 0.0064$. The results are shown in Figure 15. The bulk coefficient calculations systematically yield weaker fluxes than all the others. The Bourassa fluxes are systematically stronger than the UWPBL fluxes. (Note, however, that the Bourassa parameterization was developed for observed winds complemented by capillary and gravity wave information, and not for model winds (Mark Bourassa, personal communication). An ideal use of this parameterization would require that it be integrated in equation (7) when the original pressure swaths are derived from QS winds.) The ECMWF stress is weaker, sensible heat flux similar, and

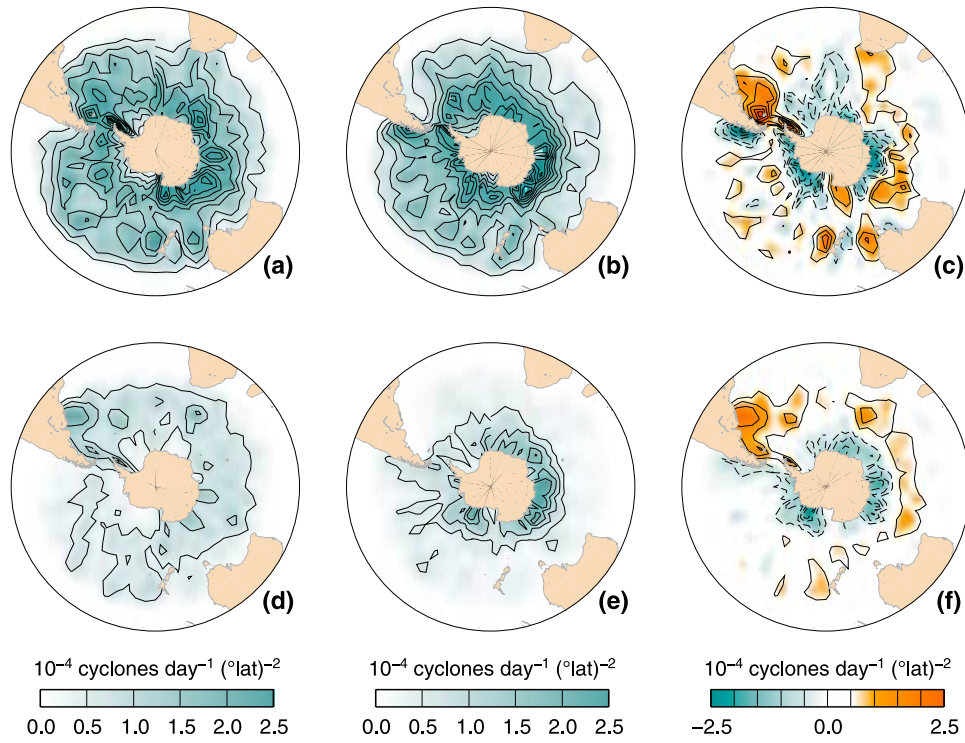


Figure 13. (a and d) Cyclogenesis, (b and e) cyclolysis, and (c and f) difference between cyclogenesis and cyclolysis for (top) short-lived versus (bottom) long-lived midlatitude cyclones, averaged over the 2000–2005 period.

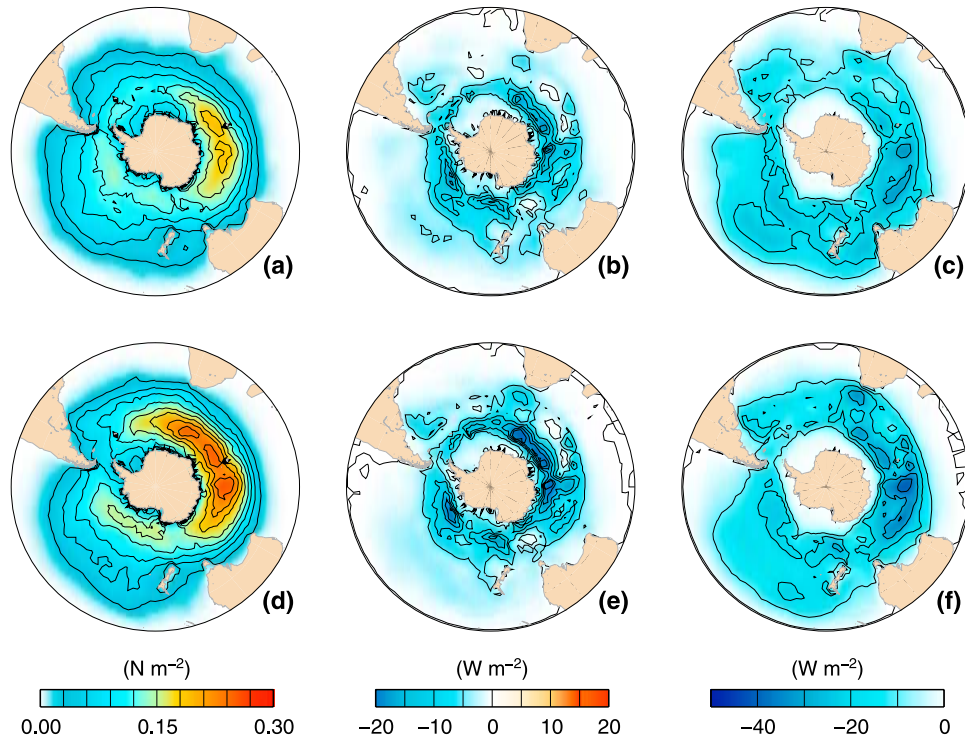


Figure 14. Winter mean flux contribution of (top) short-lived versus (bottom) long-lived midlatitude cyclones. (a and d) Stress magnitude. (b and e) Sensible heat flux. (c and f) Latent heat flux.

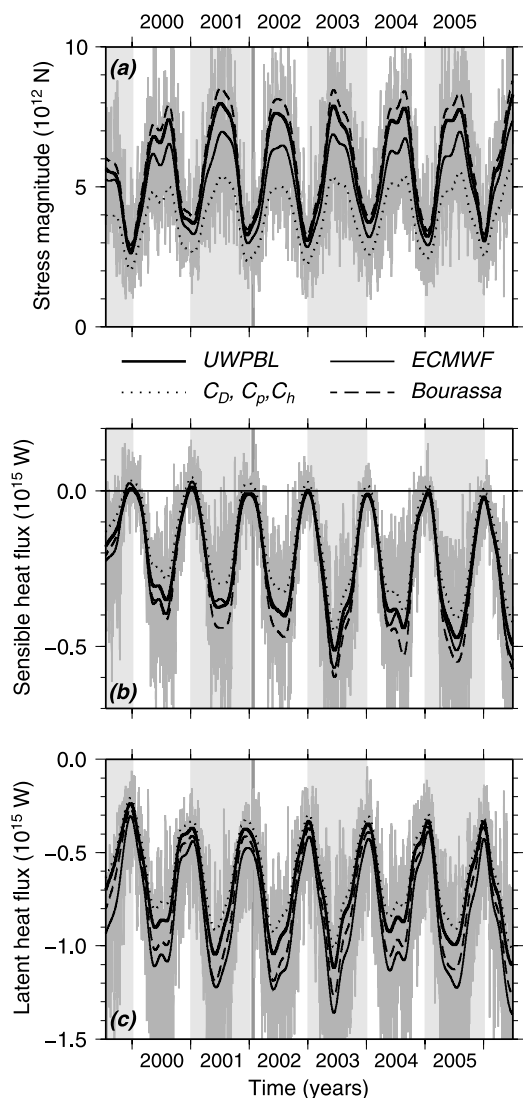


Figure 15. Comparison of spatially integrated fluxes in cyclones calculated using the UWPBL model (thick solid line), ECMWF analyses (thin solid line), standard bulk coefficients (dotted line), and Bourassa parameterization (dashed line). (a) Stress magnitude. (b) Sensible heat flux. (c) Latent heat flux.

latent heat flux stronger than the UWPBL fluxes. The differences are overall magnified in winter. Importantly, the differences are of the same order of magnitude as those found between the two SLP products presented in this article (and shown in Figure 10).

6. Concluding Discussion

[32] By injecting scatterometer information into ECMWF analyses with a wavelet method, we have shown that the scatterometer positively impacts the number and length of Southern Ocean midlatitude cyclone tracks, as well as the statistics and the geographical distribution of cyclone characteristics such as radius, depth, and cyclogenesis/lysis. When calculating the associated fluxes, we observed a modification of the spatially integrated (up to 7.8% for momentum in

cyclones) as well as spatially averaged fluxes (up to 4.6% for momentum in cyclones). Note that, as explained by PYL, the injection of scatterometer information into the ECMWF analyses has its own limitations. In particular, inherent to the pressure retrieval from the scatterometer winds is a certain amount of smoothing, which will tend to reduce the strength of the winds, and will therefore impact the calculation of the fluxes. Additionally, the injection of scatterometer-derived high-wavenumber pressure variability by wavelet decomposition only partially, due mainly to the choice of wavenumber threshold when swapping wavelet coefficients and to time lags, as well as edge effects. Should the scatterometer-pressure fields be fully assimilated using a variational method such as 3DVAR, the impact on the associated fluxes is expected to be even stronger.

[33] A differentiation of the results by cyclone type showed that mesoscale cyclones (here defined as lasting less than 4 days) represent about 75% of all cyclone tracks and 60% of all storm positions. Large storms (lasting 4 days or longer) are generated in both the polar regions and the mid-latitudes, but most of them die over the polar seas, resulting in net cyclogenesis in the midlatitudes and net cyclolysis at high latitude. Mesoscale cyclones, however, tend to both be generated and die more over polar waters than in the midlatitudes. This suggests that midlatitude cyclones likely possess more energy or can draw more energy from the ocean than cyclones generated at high latitude, which allows them to grow larger and last longer. On the other hand, cyclones generated over the polar seas cannot draw sufficient energy from the cold ocean to develop into large storms; they therefore die locally. More mesoscale cyclones are formed in the sectors of the Antarctic located south of Australia and in the Southern Indian Ocean, where the ACC is closer to Antarctica than in any other regions, as shown by *Hoskins and Hodges* [2005]. This geographic distribution of Antarctica and the ACC provides stronger meridional thermal gradients (i.e., baroclinicity) than any other location in the Southern Ocean, which is likely one of the causes for enhanced cyclogenesis in the region. However, this region is also a graveyard for both types of cyclones. Why cyclones die preferentially there remains unresolved and needs further investigation.

[34] Because the ocean gains heat in the warm sector and loses heat in the cold sector of a storm, the net sensible and latent heat fluxes due to cyclone activity are less than the fluxes for the whole ocean under all weather conditions, even though the wind stress is much stronger within cyclones. Most importantly, because they are so numerous, transient and small mesoscale cyclones contribute an amount of sensible and latent heat fluxes at the air-sea interface that is comparable to that of larger storms. A correct representation of mesoscale cyclones in NWP models is therefore critical. The research presented here indicates that oceanic SLP fields derived from satellite wind observations can enhance the detection of mesoscale cyclones, which in turn might provide better flux estimates for future climate studies, when the satellite data record becomes sufficiently long.

[35] We also noted some interannual variability, which we were not able to assign exclusively to any of three possible causes: assimilation of scatterometer data by ECMWF in 2002,

upgrades to the ECMWF NWP model, or natural variability of the Southern Ocean/atmosphere system. *Simmonds and Keay* [2000a], *Simmonds* [2003] and *Simmonds et al.* [2003] observed long-term trends in the number of Southern Hemisphere cyclones and proposed that the decreasing number of cyclones observed from about 1970 to the late 1990s could be linked to a warming hemisphere and midlatitude cyclones that are more efficient at transporting heat poleward. Using a high-resolution general circulation model (GCM), *Geng and Sugi* [2003] showed that the decrease in cyclone density might be due to a decrease in baroclinicity caused by an increase in static stability associated with enhanced greenhouse gases and sulfate aerosols. A number of authors have also reported on the so-called “Antarctic annular mode” of variability between midlatitudes and high latitudes [e.g., *Thompson and Wallace*, 2000] as well as the semiannual oscillation (SAO) [e.g., *Walland and Simmonds*, 1999] both operating on a range of timescales. In turn, the fluxes of heat and momentum between the atmosphere and the Southern Ocean might feed back on the SAO and cause part of its low-frequency variability [*Simmonds and Walland*, 1998]. The interannual variability observed in Figure 9 might also be linked to the ENSO-related variability in the number of cyclones and background pressure [*Simmonds et al.*, 2003; *White and Simmonds*, 2006]. With the 7-year record used in this study, however, the interannual and decadal atmospheric variabilities can hardly be isolated. It is even harder to disentangle these variabilities from NWP model upgrades and improvements in satellite data availability and assimilation. Since QS is still furnishing wind measurements, our statistics will improve as we use a longer data record.

[36] **Acknowledgments.** We would like to thank Mark Bourassa for providing us with his flux calculation scheme and Joey Comeaux at the National Center for Atmospheric Research for his help in using the ds111.3 ECMWF products, as well as two anonymous reviewers for their careful and constructive review of this article. The ds111.3 data were provided by ECMWF through the Data Support Section of the Computational and Information Systems Laboratory at NCAR. NCAR is supported by grants from the National Science Foundation. Yuan was supported by the National Science Foundation through grants OPP02300284 and ANT 07-32656. Li was supported by NASA OVVST through grant JPLCIT-1216483. Patoux acknowledges NASA OVVST grant support under JPL subcontract 1285663. Lamont publication 7227.

References

- Blechschmidt, A.-M. (2008), A 2-year climatology of polar low events over the Nordic Seas from satellite remote sensing, *Geophys. Res. Lett.*, *35*, L09815, doi:10.1029/2008GL033706.
- Bourassa, M. (2006), Satellite-based observations of surface turbulent stress during severe weather, *Atmosphere-Ocean Interactions*, vol. 2, edited by W. Perrie, pp. 35–52, Wessex Inst. of Technol. Press, Southampton, U.K.
- Bromwich, D. H., and T. R. Parish (1998), Meteorology of the Antarctic, in *Meteorology of the Southern Hemisphere*, edited by D. Koroly and D. Vincent, chap. 4, pp. 175–200, Am. Meteorol. Soc., Boston, Mass.
- Brown, R. A., and G. Levy (1986), Ocean surface pressure fields from satellite sensed winds, *Mon. Weather Rev.*, *114*, 2197–2206.
- Brown, R. A., and W. T. Liu (1982), An operational large-scale marine planetary boundary layer model, *J. Appl. Meteorol.*, *21*, 261–269.
- Brown, R. A., and L. Zeng (1994), Estimating central pressures of oceanic mid-latitude cyclones, *J. Appl. Meteorol.*, *33*, 1088–1095.
- Carleton, A. M. (1995), On the interpretation and classification of meso-scale cyclones from satellite infrared imagery, *Int. J. Remote Sens.*, *16*, 2457–2485.
- Carleton, A. M., and D. A. Carpenter (1990), Satellite climatology of polar lows and broadscale climatic associations for the Southern Hemisphere, *Int. J. Climatol.*, *10*, 219–246.
- Carleton, A. M., and Y. Song (1997), Synoptic climatology, and intrahemispheric associations, of cold air mesocyclones in the Australasian sector, *J. Geophys. Res.*, *102*, 13,873–13,887.
- Carrasco, J. F., and D. H. Bromwich (1993), Mesoscale cyclogenesis dynamics over the Southwestern Ross Sea, Antarctica, *J. Geophys. Res.*, *98*, 12,973–12,995.
- Condron, A., G. R. Bigg, and I. A. Renfrew (2006), Polar mesoscale cyclones in the northeast Atlantic: Comparing climatologies from ERA-40 and satellite imagery, *Mon. Weather Rev.*, *134*, 1518–1533.
- Fairall, C. W., E. F. Bradley, J. E. Hare, A. A. Grachev, and J. B. Edson (2003), Bulk parameterization of air-sea fluxes: Updates and verification for the COARE algorithm, *J. Clim.*, *16*, 571–591.
- Fitch, M., and A. M. Carleton (1992), Antarctic mesocyclone regimes from satellite and conventional data, *Tellus, Ser. A*, *44*, 180–196.
- Geng, Q., and M. Sugi (2003), Possible change of extratropical cyclone activity due to enhanced greenhouse gases and sulfate aerosols-study with a high-resolution AGCM, *J. Clim.*, *16*, 2262–2274.
- Godfred-Spinning, C. R., and I. Simmonds (1996), An analysis of Antarctic sea ice and extratropical cyclone associations, *Int. J. Climatol.*, *16*, 1315–1332.
- Hilburn, K. A., M. A. Bourassa, and J. O’Brien (2003), Development of scatterometer-derived research-quality surface pressures for the Southern Ocean, *J. Geophys. Res.*, *108*(C7), 3244, doi:10.1029/2003JC001772.
- Hoskins, B. J., and K. Hodges (2005), A new perspective on Southern Hemisphere storm tracks, *J. Clim.*, *18*, 4108–4129.
- Kelly, K., S. Dickinson, M. McPhaden, and G. Johnson (2001), Ocean currents evident in satellite wind data, *Geophys. Res. Lett.*, *28*, 2469–2472.
- Kubota, M., A. Kano, H. Muramatsu, and H. Tomita (2003), Intercomparison of various latent heat flux fields, *J. Clim.*, *16*, 670–678.
- Liu, W. T., K. B. Katsaros, and J. A. Businger (1979), Bulk parameterization of air-sea exchanges of heat and water vapor including the molecular constraints at the interface, *J. Atmos. Sci.*, *36*, 1722–1735.
- Marshall, G., and J. Turner (1997), Surface wind fields of Antarctic mesocyclones derived from ERS 1 scatterometer data, *J. Geophys. Res.*, *102*, 13,907–13,921.
- McMurdie, L. A., C. Claud, and S. Atakturk (1997), Satellite-derived atmospheric characteristics of spiral and comma-shaped Southern Hemisphere mesocyclones, *J. Geophys. Res.*, *102*, 13,889–13,905.
- Murray, R. J., and I. Simmonds (1991), A numerical scheme for tracking cyclone centres from digital data. Part II: Application to January and July General Circulation Model simulations, *Aust. Meteorol. Mag.*, *39*, 167–180.
- Patoux, J. (2004), UWPBL 4.0, the University of Washington Planetary Boundary Layer (UWPBL) model, report, 77 pp., Univ. of Wash., Seattle. (Available at ftp://eos.atmos.washington.edu/pub/UWPBL/doc.pdf)
- Patoux, J., X. Yuan, and C. Li (2009), Satellite-based midlatitude cyclone statistics over the Southern Ocean: I. Scatterometer-derived pressure fields and storm tracking, *J. Geophys. Res.*, *114*, D04105, doi:10.1029/2008JD010873.
- Peixoto, J. P., and A. H. Oort (1992), *Physics of Climate*, 520 pp., Am. Inst. of Phys., College Park, Md.
- Rasmussen, E. A., and J. Turner (2003), *Polar Lows: Mesoscale Weather Systems in the Polar Regions*, 612 pp., Cambridge Univ. Press, Cambridge, U.K.
- Rouault, M., C. J. C. Reason, J. R. E. Lutjeharms, and A. C. M. Beljaars (2003), Underestimation of latent and sensible heat fluxes above the Agulhas Current in NCEP and ECMWF analyses, *J. Clim.*, *16*, 776–782.
- Simmonds, I. (2003), Modes of atmospheric variability over the Southern Ocean, *J. Geophys. Res.*, *108*(C4), 8078, doi:10.1029/2000JC000542.
- Simmonds, I., and K. Keay (2000a), Variability of Southern Hemisphere extratropical cyclone behavior, 1958–97, *J. Clim.*, *13*, 550–561.
- Simmonds, I., and K. Keay (2000b), Mean Southern Hemisphere extratropical cyclone behavior in the 40-year NCEP-NCAR reanalysis, *J. Clim.*, *13*, 873–885.
- Simmonds, I., and K. Keay (2002), Surface fluxes of momentum and mechanical energy over the North Pacific and North Atlantic oceans, *Meteorol. Atmos. Phys.*, *80*, 1–17.
- Simmonds, I., and R. J. Murray (1999), Southern extratropical cyclone behavior in ECMWF analyses during the FROST special observing periods, *Weather Forecasting*, *13*, 878–891.
- Simmonds, I., and D. Walland (1998), Decadal and centennial variability of the southern semiannual oscillation simulated in the GFDL coupled GCM, *Clim. Dyn.*, *14*, 45–53.
- Simmonds, I., R. J. Murray, and R. M. Leighton (1999), A refinement of cyclone tracking methods with data from FROST, *Aust. Meteorol. Mag.*, June special, 35–49.
- Simmonds, I., K. Keay, and E.-P. Lim (2003), Synoptic activity in the seas around Antarctica, *Mon. Weather Rev.*, *131*, 272–288.
- Thompson, D., and J. Wallace (2000), Annular modes in the extratropical circulation. Part I: Month-to-month variability, *J. Clim.*, *13*, 1000–1016.
- Walland, D., and I. Simmonds (1999), Baroclinicity, meridional temperature gradients, and the southern semiannual oscillation, *J. Clim.*, *12*, 3376–3382.

White, W., and I. Simmonds (2006), Sea surface temperature-induced cyclogenesis in the Antarctic circumpolar wave, *J. Geophys. Res.*, *111*, C08011, doi:10.1029/2004JC002395.

Yuan, X. (2004), High-wind-speed evaluation in the Southern Ocean, *J. Geophys. Res.*, *109*, D13101, doi:10.1029/2003JD004179.

Yuan, X., D. J. Martinson, and W. T. Liu (1999), The effect of air-sea interaction on winter 1996 Southern Ocean subpolar storm distribution, *J. Geophys. Res.*, *104*, 1991–2007.

C. Li and X. Yuan, Lamont-Doherty Earth Observatory, Columbia University, 61 Route 9W, P.O. Box 1000, Palisades, NY 10964, USA. (xyuan@ldeo.columbia.edu)

J. Patoux, Department of Atmospheric Sciences, University of Washington, 408 ATG Building, Seattle, WA 98195-1640, USA. (jerome@atmos.washington.edu)